Protease-Sensitive, VEGF-Mimetic Peptide, and IKVAV Laminin-Derived Peptide Sequences within Elastin-Like Recombinamer Scaffolds Provide Spatiotemporally Synchronized Guidance of Angiogenesis and Neurogenesis

Fernando González-Pérez, Matilde Alonso, Israel González de Torre, Mercedes Santos, and José Carlos Rodríguez-Cabello*

Spatiotemporal control of vascularization and innervation is a desired hallmark in advanced tissue regeneration. For this purpose, we design a 3D model scaffold, based on elastin-like recombinamer (ELR) hydrogels. This contains two interior and well-defined areas, small cylinders, with differentiated bioactivities with respect to the bulk. Both are constructed on a protease sensitive ELR with a fast-proteolyzed domain, but one bears a VEGF-mimetic peptide (QK) and the other a laminin-derived pentapeptide (IKVAV), to promote angiogenesis and neurogenesis, respectively. The outer bulk is based on a slow proteolytic sequence and RGD cell adhesion domains. In vitro studies show the effect of QK and IKVAV peptides on the promotion of endothelial cell and axon spreading, respectively. The subcutaneous implantation of the final 3D scaffold demonstrates the ability to spatiotemporally control angiogenesis and neurogenesis in vivo. Specifically, the inner small cylinder containing the QK peptide promotes fast endothelialization, whereas the one with IKVAV peptide promotes fast neurogenesis. Both, vascularization and innervation take place in advance of the bulk scaffold infiltration. This scaffold shows that it is possible to induce vascularization and innervation in predetermined areas of the scaffold well ahead to the bulk infiltration. That significantly increases the efficiency of the regenerative activity.

F. González-Pérez, M. Alonso, I. González de Torre, M. Santos, J. C. Rodríguez-Cabello
G.I.R. BIOFORGE (Group for Advanced Materials and Nanobiotechnology)
CIBER-BBN
Edificio LUCIA
Universidad de Valladolid
Paseo Belén 19, Valladolid 47011, Spain
E-mail: roca@bioforge.uva.es

1. Introduction

Tissue engineering and regenerative medicine (TERM) strategies aimed at obtaining a substitute that faithfully reproduces the functionality of damaged tissues rely on two major processes: angiogenesis and, often-overlooked, neurogenesis. Angiogenesis is a complex process that comprises degradation of the extracellular matrix (ECM) upon the release of proteases by endothelial cells,[1] followed by their proliferation and growth, to create a functional capillary network that restores the supply of nutrients and oxygen exchange that is essential for cell survival.[2] In contrast, neurogenesis involves the release of proteases by neural progenitor cells,[3] axonal growth, and proliferation of Schwann cells, which subsequently perform remyelination, to reform neural circuits that both restore the lost host-mediated motor and sensory functions and,[4] more importantly during the initial stages of regeneration, shows specific signaling that promotes mesenchymal cell proliferation and regeneration.[5] As such, a lack of these cells impairs cell proliferation and wound healing, while their expansion promotes cell differentiation and tissue formation. Thus, injury-activated glia and/or their secretome have therapeutic potential in regenerative approaches.[6] In this sense, the combined and advanced spatiotemporal guidance of novel vascular and neural systems seems to work in a synergistic manner to adequately biomimic complex, native, 3D organizational processes and enhance tissue regeneration. This synergistic approach could therefore allow the successful restoration of tissue and organ function and the long-term stability of the scaffold within the host tissue.[6,7]

One potential solution involves the encapsulation of multiple growth factors (GFs) and inhibitors, such as vascular endothelial growth factor (VEGF), nerve growth factor (NGF) or anti-VEGF, in complex protease-sensitive hydrogels.[4c,8] However, these loading strategies lack precise control over the gradient distribution and release pharmacokinetics of GFs, which

may result in dose-related adverse effects, such as undesired immune responses or cytotoxic effects.[9] Another approach to obtain oriented nerve tissue involves the use of laminin-derived peptides, which contribute to neural attachment and outgrowth, thereby promoting neurogenesis.[10] Although some studies have achieved axonal guidance during neural development, light or temperature gradients needed to be applied to the surface.[11] Thus, novel systems that enable the availability of GF, cell-adhesiveness, and cleavage kinetics in order to spatiotemporally direct the angiogenesis and neurogenesis events are required.[7]

Genetically engineered polypeptides, in particular those inspired by the intrinsically disordered regions of native elastin, represent a versatile platform in this regard.[12] The amino-acid sequence of this family of proteins, known as elastin-like recombinamers (ELRs) when they are produced recombinantly, can be fine-tuned to encode and tether the required bioactive domains while preserving the reversible lower critical solution temperature (LCST) in aqueous phase.[13] They can prevent fibrotic tissue formation and enhance wound healing via modulation of the innate immune response towards anti-inflammatory type-2 macrophages (M2).[14] In addition, ELRs can be decorated with cross-linkable groups to provide hydrogel-like scaffolds. The strain-promoted [3 + 2] azide-alkyne cycloaddition (SPAAC) was selected for this study,[15] as this reaction has been shown to provide a fast, cytocompatible and catalyst-free orthogonal approach to physiological environments in living organisms.[16]

In this regard, several novel strategies have explored the combination of ELR hydrogels with proangiogenic peptides for the promotion of angiogenesis. For example, the attachment of the QK peptide (KLTWQELYQLKYKGI), a VEGF-mimetic peptide, to an ELR hydrogel bearing Arg-Gly-Asp (RGD) cell-adhesion motifs allowed the formation of capillaries in vivo.[17] This approach was found to satisfactorily provide the required signaling by addressing the unwanted gradients exhibited by common cargo delivery approaches, which may lead to a lack of reproducibility and possible toxic effects.[18] With regard to the promotion of neurogenesis, the Ile-Lys-Val-Ala-Val (IKVAV) neurite cell adhesion sequence, and the RGD cell adhesion sequence, have also shown promising results when incorporated into ELRs.[19] Thus, Pavia Dos Santos et al. developed an IKVAV-containing ELR hydrogel that supported sensory neurons outgrowth and promoted the formation of nerve terminations upon subcutaneous implantation in mice.[19a] Similarly, Straley et al. described that increasing the RGD density within ELR hydrogels led to an increase in neurite cell adhesion together with more extensive outgrowth.[19b] On the other hand, the incorporation of labile domains sensitive to the urokinase plasminogen activator (uPA) enzyme within ELR sequences has shown promising results in the spatiotemporal guidance of angiogenesis. As such, fast and slow degradable uPA-protease-sensitive sequences, namely Gly-Thr-Ala-Arg (GTAR) and Asp-Arg-Ile-Arg (DRIR), respectively, have been employed to fabricate a sandwich-like ELR scaffold that allowed anisotropic colonization in vivo.[20] A subsequent approach combined the QK proangiogenic factor and the same uPA-protease-sensitive fast (GTAR) and slow (DRIR) domains in the inner (fast) and outer part (slow) of a coaxial binary ELR cylindrical construct. This approach demonstrated a two-step process involving cell infiltration and subsequent vascularization of the inner part of the construct followed by progressive invasion of the outer part, thus allowing the spatiotemporal guidance of angiogenesis in vivo.[14a] In terms of neurogenesis, the uPA enzyme member of the serine-protease family has been reported to be expressed and released from the tips of growing neurons and oligodendrocytes during development of the rat brain, thereby playing a key role in axonal growth and in vivo nerve regeneration.[21]

In light of the above, we hypothesize that the integration of i) the VEGF-mimetic peptide (QK), ii) the neurite cell-adhesive sequence (IKVAV), iii) the RGD integrin-binding domain, and iv) the fast and slow uPA-protease-sensitive epitopes in a single ELR scaffold may serve to encode the optimal spatiotemporal control of angiogenesis and neurogenesis in vivo. In order to assess this hypothesis, we designed an ELR scaffold containing two small longitudinal and internal cylinders bearing the VEGF-mimetic peptide (QK) and the neurite cell-adhesion domain (IKVAV), respectively, to independently and simultaneously promote and guide early angiogenesis and neurogenesis. These internal cylinders are based on GTAR-ELR and RGD-ELR, which bear the fast-degrading uPA-protease-sensitive (GTAR) and the cell-adhesive RGD domain covalently decorated with the QK and IKVAV bioactive molecule, respectively. The external part of this 3D model ELR scaffold consists of the slow-protease-sensitive DRIR-ELR and RGD-ELR pair. The non-protease-sensitive VKV-N$_3$-ELR and VKV-Cy-ELR pair was used in the outer part as control. We propose that the designed constructs may allow the spatiotemporal guidance of angiogenesis and neurogenesis in a pre-defined orientation and time, in contrast to uniform hydrogels, where colonization and subsequent vascular and neuronal formation usually progresses slowly from the scaffold surface.

Initial mechanical and morphological studies were performed to evaluate the applicability of the 3D model ELR scaffolds for soft-tissue regeneration. In vitro studies were then used to assess the bioactivity of the ELR hydrogels against neuronal and endothelial cells. Finally, the designed 3D model ELR scaffolds, as well as their constituent parts, i.e., the independent ELR hydrogels, were implanted subcutaneously in mice. Histological and immunohistochemical evaluation was performed after 2, 4, and 6 weeks to assess the ability of the scaffolds to spatiotemporally control the angiogenesis and neurogenesis processes in vivo by forming functional capillaries and peripheral nerves in the interior of the scaffold and in advance to the bulk of cell colonization.

2. Results and Discussion

2.1. Rheological Characterization of ELR Hydrogels

The mechanical properties of the ELR hydrogels produced at 50 mg mL^{-1} were determined in the linear viscoelastic region for use in TERM. A strain sweep measurement of nonprotease-sensitive, slow, fast, fast-QK, and fast-IKVAV ELR hydrogels (composition detailed in Table S1 Supporting Information) demonstrated no correlation between the complex modulus (|G^*|) and the strain amplitude (Figures S1–S5, Supporting Information). The complex modulus of ELR hydrogels at a frequency of 1 Hz, 1% strain, and 37 °C (represented in **Figure 1**) showed no statistically significant differences. In addition, the values measured in the range 1214 ± 26 Pa were in accordance with the efficient stiffness reported for optimal neuronal outgrowth and soft-tissue applications.[15a,22]
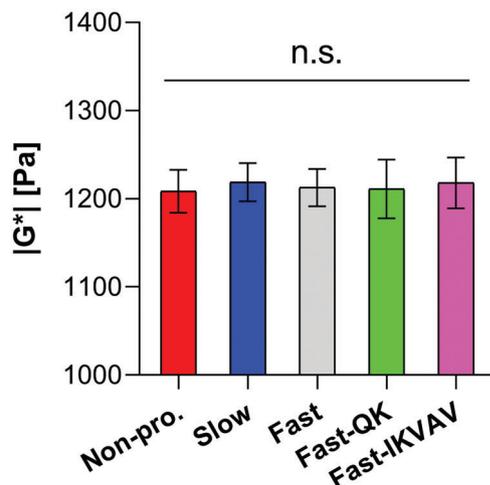
ADVANCED
SCIENCE NEWS

www.advancedsciencenews.com

**ADVANCED
HEALTHCARE
MATERIALS**

www.advhealthmat.de

Figure 1. Complex elastic modulus $|G^*|$ for non-protease-sensitive (non-pro.), slow, fast, fast-QK and fast-IKVAV ELR hydrogels evaluated at 1 Hz, 1% strain and 37 °C, represented as mean ± SD. n.s. stands for $p > 0.05$.

2.2. Morphology of ELR Hydrogels

Scanning electron microscopy (SEM) images and the percentage gel hydration for nonprotease-sensitive, slow, fast, fast-QK, and fast-IKVAV ELR hydrogels at 50 mg mL^{-1} are shown in **Figure 2**. All scaffolds exhibit an interconnected porous structure, with a pore size of 8 ± 2 µm and a hydration value of 60 ± 6% (Figure 2), with no statistically significant differences between them. The microstructure is in accordance with similar scaffolds designed for soft tissue engineering purposes, thereby supporting the potential applicability of the manufactured ELR hydrogels for the intended purpose.[14a,15a,23]

2.3. In Vitro Morphogenesis Analysis of C6 Glial Cells Top-Seeded onto ELR Hydrogels

The effect of nonprotease-sensitive, slow, fast, fast-QK, and fast-IKVAV ELR hydrogels on neurite outgrowth was evaluated in an in vitro top-seeded 2D culture study with C6 glial cells. After 24 h, ELR hydrogels showed an initial attachment of glial cells accompanied by a small neurite extension upon staining with phalloidin (actin filaments) and counterstaining with DAPI (nuclei marker). At 48 h, slow, fast, fast-QK, and fast-IKVAV ELR hydrogels exhibited a significant increase in axonal length compared with the nonprotease-sensitive hydrogel lacking the RGD cell-adhesion motifs. Furthermore, neurite extension was much more noticeable in the hydrogel bearing the IKVAV domain, thus suggesting that the IKVAV peptide favors the axonal growth of C6 glial cells (**Figure 3**). This trend was maintained over time. Thus, after 72 h, the nonprotease-sensitive hydrogel showed lower neurite extensions than the RGD-containing hydrogels, observing the highest values in the presence of the fast-IKVAV hydrogel (102 ± 21 µm). These findings confirm the proneurogenesis specificity induced by the IKVAV peptide over neurite adaptation and outgrowth, thereby supporting the bioactivity displayed by polylysine and poly(ethylene glycol) (PEG) ELR IKVAV-containing hydrogels.[10b,19]

2.4. In Vitro Morphogenesis Analysis of Human Umbilical Vein Endothelial Cells (HUVECs) Top-Seeded onto ELR Hydrogels

The proangiogenic effect of non-protease-sensitive, slow, fast, fast-QK, and fast-IKVAV ELR hydrogels was analyzed in an in vitro top-seeded 2D HUVECs adhesion study. After 2 h, phalloidin (actin filaments) staining and DAPI (nuclei marker) counterstaining revealed an initial cell attachment for all the ELR hydrogels except for the non-protease-sensitive (**Figure 4**). This behavior correlated with the presence or absence of RGD cell-adhesion motifs.[14a,24] At 6 h, the fast-QK ELR hydrogel showed cells with elongated morphology and sprouting, tending to anastomosis (formation of networks and branching). This contrasted with the slow, fast, and fast-IKVAV ELR hydrogels where cells showed a cobblestone morphology, and with the non-protease-sensitive ELR hydrogel where the absence of RGD motifs delayed cell adhesion (Figure 4). At the last time point evaluated, HUVECs maintained the same low adhesion, cobblestone, or filamentous morphology observed at 6 h for the respective non-protease-sensitive, slow, fast, and fast-QK ELR hydrogels. On the other hand, the fast-IKVAV ELR hydrogel showed an increase in cell spreading and anastomosis (Figure 4). These results confirm the proangiogenic activity of the fast-QK ELR hydrogel, and suggest a proangiogenic effect of the fast-IKVAV ELR hydrogel. Thus, in accordance with previously reported in vitro HUVEC studies where the incorporation of IKVAV peptide showed to enhance cell attachment and induce a more spindle-shaped morphology than RGD containing hydrogels.[14a,25]

2.5. In Vivo Study of ELR Hydrogels

The onset of angiogenesis and neurogenesis was evaluated in vivo by subcutaneous implantation of non-protease-sensitive, slow, fast, fast-QK, and fast-IKVAV ELR hydrogels in mice. The macroscopic evaluation of ELR hydrogels after 6 weeks showed no marked inflammation in the implantation area, along with the presence of surrounding blood vessels and an absence of fibrotic tissue, in agreement with previous studies (**Figure 5**a).[14a] Hematoxylin and eosin (H&E) staining revealed that the structure of the ELR hydrogels was conserved after 2 weeks, with this being maintained over time for the non-protease-sensitive ELR hydrogels (Figure 5b). This trend contrasted with the slow, fast, fast-QK and fast-IKVAV ELR hydrogels, which showed advanced states of colonization after 4 and 6 weeks. Slow ELR hydrogels preserved the largest area at each time point, followed by the fast ELR hydrogels and the QK- and IKVAV-containing hydrogels, which exhibited almost complete invasion after 6 weeks (Figure 5b). DAPI counterstaining (nuclei marker) was performed to analyze the cell infiltration rate within the different ELR hydrogels (Figure 5b). Quantification of the nuclei revealed a significantly lower cell density for the non-protease-sensitive ELR hydrogels, which remained throughout the study. On the other hand, slow ELR hydrogels showed a moderate colonization, with cells preferentially located on the surface of the scaffold. This contrasts with fast, fast-QK and fast-IKVAV ELR hydrogels, the core of which appeared to be further colonized at 4 weeks postimplantation (Figure 5b). In particular, the fast-QK and fast-IKVAV ELR hydrogels showed
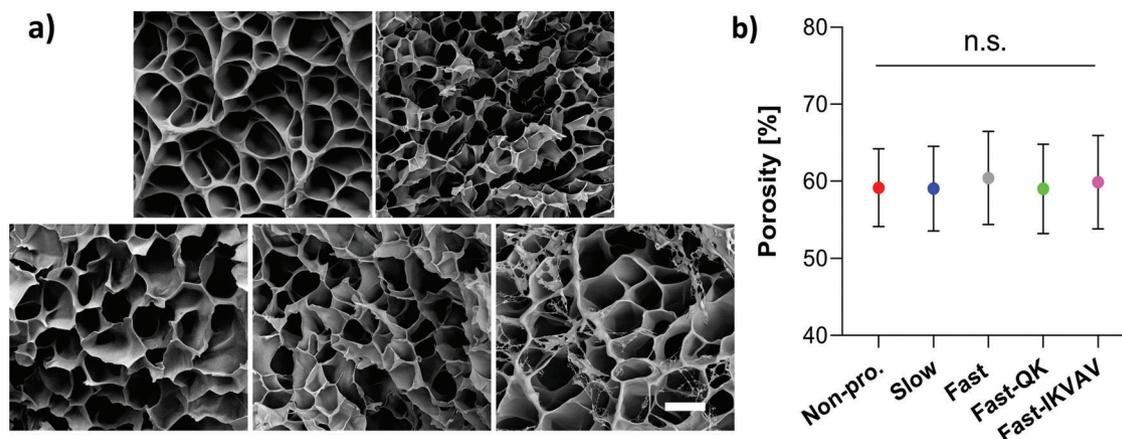
**ADVANCED
SCIENCE NEWS**

www.advancedsciencenews.com

**ADVANCED
HEALTHCARE
MATERIALS**

www.advhealthmat.de

Figure 2. a) Representative SEM micrographs of cryo-fractured, lyophilized and gold-sputtered cross-sections of the non-protease-sensitive (Non-pro.) and slow (from left to right on the first row), and fast, fast-QK and fast-IKVAV (from left to right on the second row) ELR hydrogels. Scale bar = 10 μm. b) Percentage of porosity for each ELR hydrogel, represented as mean ± SD. n.s. stands for p > 0.05.
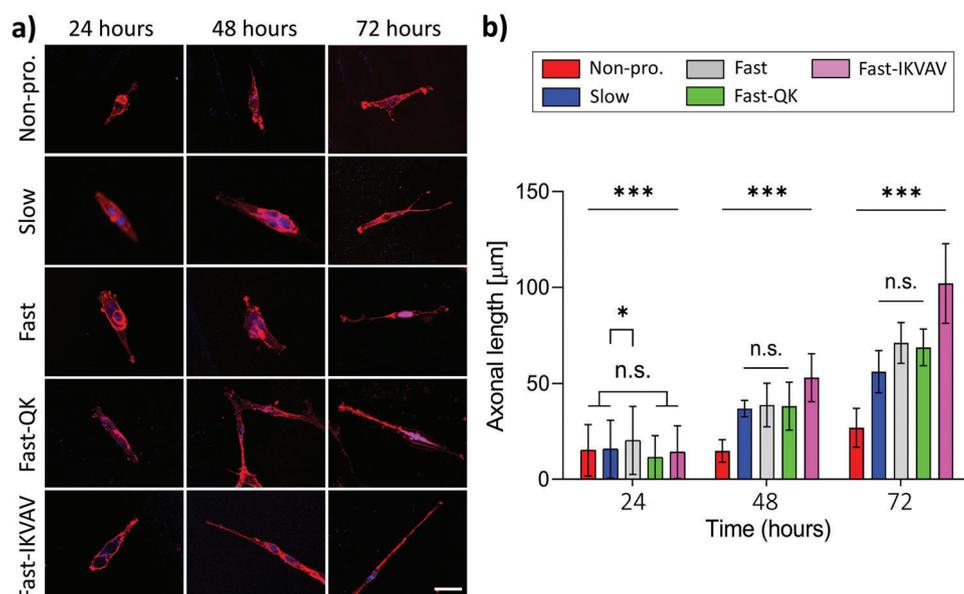

Figure 3. a) Representative confocal images of C6 glial cells top-seeded onto individual non-protease-sensitive (Non-pro.), slow, fast, fast-QK and fast-IKVAV ELR hydrogels stained with phalloidin for actin filaments (red) and counterstained with DAPI for nuclei (blue), after 24, 48 and 72 h. Columns refer to the different time points, whereas rows refer to hydrogels. Scale bar = 25 μm. b) Axonal length of C6 glial cells top-seeded onto ELR hydrogels after 24, 48 and 72 h. Some statistical differences are not shown for clarity. Data are reported as mean ± SD. (***) p < 0.001, (**) p < 0.01, (*) p < 0.05 and (n.s.) no significant differences.

the highest cell-colonization rates, with no significant differences between them at any time, thus confirming that both bioactive domains provide a similar synergistic effect together with uPA-protease-sensitive domains on the cell-infiltration rate (Figure 5c). Furthermore, CD31 (endothelial marker) and β-III tubulin (neural marker) immunostaining was performed to evaluate the angiogenesis and neurogenesis process within the ELR hydrogels. The non-protease-sensitive ELR hydrogels revealed a markedly lower number of endothelial and neuronal cells at every time point (Figure 5b,c), whereas slow and fast ELR hydrogels showed a reduced number of capillaries, with no significant differences between them after 4 weeks. This contrasts

with the findings for the fast-QK and fast-IKVAV ELR hydrogels at this time, which indicated the onset of the angiogenesis process at the surface, with the QK-containing hydrogel showing the highest number of capillaries. The preferred formation of capillaries, exhibited by the Fast-QK ELR hydrogel, continued after 6 weeks, with this trend being followed by the fast-IKVAV and fast and slow ELR hydrogels, respectively (Figure 5b,c). This confirmed the synergistic effect of fast uPA-protease-sensitive sequences and QK peptide on the angiogenesis process, which also occurred with the IKVAV peptide, but to a lesser extent. In terms of neuronal infiltration, no signs of neurogenesis were observed in the ELR hydrogels until 6 weeks (Figure 5b,c). At this time, the
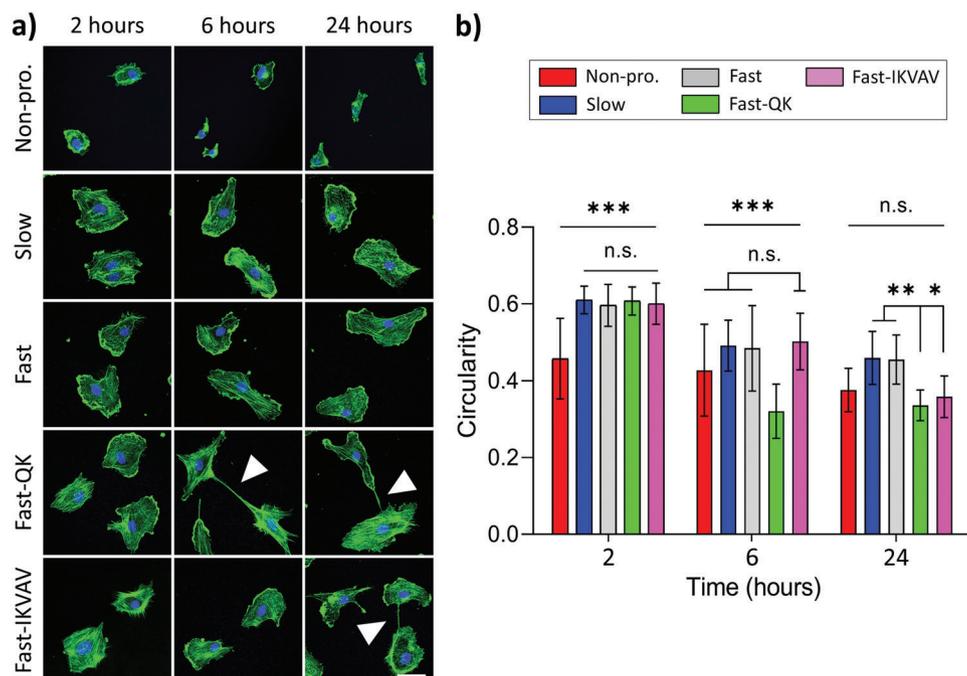
**ADVANCED
SCIENCE NEWS**

www.advancedsciencenews.com

**ADVANCED
HEALTHCARE
MATERIALS**

www.advhealthmat.de

Figure 4. a) Representative confocal images of HUVECs top-seeded onto individual non-protease-sensitive (Non-pro.), slow, fast, fast-QK and fast-IKVAV ELR hydrogels stained with phalloidin for actin filaments (green) and counterstained with DAPI for nuclei (blue), after 2, 6 and 24 h. Columns refer to the different time points, whereas rows refer to hydrogels. Scale bar = 40 μm. b) Circularity of HUVECs top-seeded onto ELR hydrogels after 2, 6 and 24 h. Some statistical differences are not shown for clarity. Data are reported as mean ± SD. (***) $p < 0.001$, (**) $p < 0.01$, (*) $p < 0.05$ and (n.s.) no significant differences.

fast-IKVAV ELR hydrogel showed the highest presence of neuronal cells and a more defined myelin sheath (Figure 5d), with more than a twofold increase in β-III tubulin stained area compared with the fast-QK ELR hydrogel ($p < 0.001$) (Figure 5b,c). Interestingly, fast and slow ELR hydrogels also showed the onset of the neurogenesis process, with neuronal cells being observed on their surface after 6 weeks (Figure 5b,c). This result confirmed the synergy between the uPA-protease-sensitive sequences and the IKVAV peptide (covalently tethered) in the promotion of neurogenesis, and the positive and synergistic effect of the QK peptide (covalently tethered) on neuronal infiltration. The inclusion of protease-sensitive domains within scaffolds has already been shown to provide positive results for the angiogenesis and neurogenesis processes in vivo. In a growth factor-free approach, Flora et al. demonstrated the impact of proteolysis rate on the vascularization process, comparing ELR hydrogels with different cleavage kinetics towards the uPA enzyme.[20] Similarly, Yiming et al. reported neuronal cell colonization accompanying vascularization on matrix metalloproteinase (MMP)-sensitive PEG hydrogels upon comparison with unmodified and hydrolytically degradable PEG hydrogels, thus highlighting the importance of tuning the sensitivity to proteases on angiogenesis and neurogenesis processes in vivo.[26] These approaches have also been improved by attaching biochemical cues, specifically the QK peptide and IKVAV neural cell adhesive sequence. As described by Leslie-Barbick et al., collagenase-degradable PEG-QK hydrogels showed an enhanced vascularization process, with a higher vessel density in vivo when compared to PEG-RGDS, PEG-VEGF, and VEGF-embedded hydrogels.[27] Likewise, Flora

et al. reported an increase in the formation of capillaries in vivo with ELR-QK hydrogels bearing REDV and RGD cell-adhesive sequences compared with factor-free ELR hydrogels.[17a] As regards the IKVAV peptide, Pavia Dos Santos et al. developed ELR-PEG-IKVAV hydrogels that showed the formation of nerve structures in vivo, in contrast to ELR-PEG-VKAIV hydrogels displaying the scrambled peptide, thus reinforcing the effect of IKVAV on neurogenesis.[19a] Although these approaches have shown promising results in terms of stimulating endothelial and neuronal cell colonization, the lack of preprogrammed cell infiltration within scaffolds can result in nonuniform cell distribution, loss of functionality, and limited long-term viability of the neotissue.[2b,7c]

2.6. In Vivo Evaluation of 3D Model ELR Scaffolds as Spatiotemporal Angiogenesis and Neurogenesis Guiding Constructs

Based on the individual ELR hydrogel findings, we designed the non-protease-sensitive/QK/IKVAV (hereinafter non-pro./QK/IKVAV) and the slow/QK/IKVAV 3D model ELR scaffolds and evaluated their applicability as spatiotemporal angiogenesis and neurogenesis guiding constructs. These new scaffolds consist of a non-protease-sensitive or a slow ELR hydrogel encompassing a pair of cylindrical fast-QK and fast-IKVAV ELR hydrogels (fabrication process and ELR hydrogels composition detailed in **Figure 6** and Table S2 Supporting Information, respectively). Macroscopic evaluation of these 3D
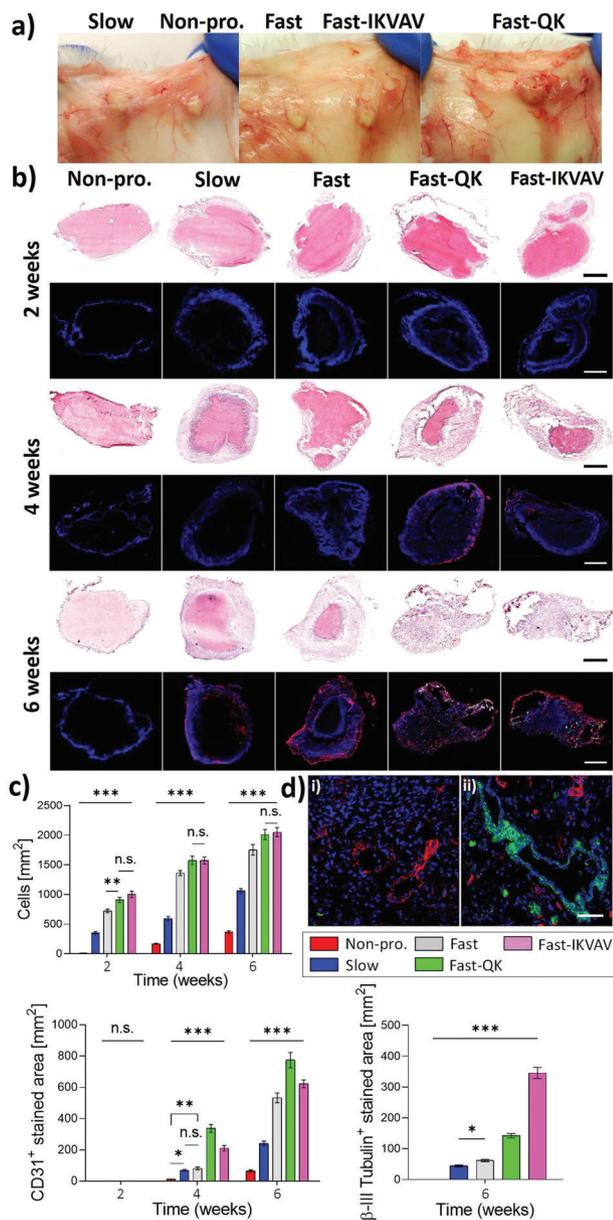
Figure 5. Analysis of individual ELR hydrogels in vivo. a) Representative images of ELR hydrogels at six weeks post-implantation in mice. b) Representative H&E-stained ELR microsections with their respective CD31 and β-III tubulin immunofluorescence staining and DAPI counterstaining in black background. Nuclei appear in blue, endothelial cells in red and neuronal cells in green. Columns correspond to the different ELR hydrogels, while rows indicate time points. Scale bar = 1 mm. c) Quantification of number of cells, CD31+-stained area and β-III tubulin+-stained area per mm² for the individual ELR hydrogels after the different time points post-implantation. d) Representative CD31 and β-III tubulin immunofluorescence staining and DAPI counterstaining zoom-in confocal images of (i) fast-QK and (ii) fast-IKVAV ELR hydrogels after six weeks. The fast-QK ELR hydrogel showed capillaries in red and the fast-IKVAV ELR hydrogel shows long peripheral nerves in green with a defined myelin sheath. Scale bar = 50 μm. Some statistically significant comparisons are not shown for clarity. Data represented as ± SD. (***) $p < 0.001$, (**) $p < 0.01$, (*) $p < 0.05$ and (n.s.) no significant differences.

scaffolds after subcutaneous implantation in mice revealed no differences compared with the single ELR hydrogels, with no marked inflammation and a number of blood vessels surrounding the scaffolds. H&E staining evidenced a preserved structure for the non-protease-sensitive/QK/IKVAV (hereinafter non-pro./QK/IKVAV) 3D scaffold after 2 weeks. In contrast, at the same time point the slow/QK/IKVAV 3D scaffold exhibited the first signs of degradation in the inner cylinders bearing the fast-QK and fast-IKVAV hydrogels, as well as at the surface of the 3D scaffold bearing the slow ELR hydrogel (**Figure 7**a). This trend continued over time. Thus, after 4 weeks, a higher degradation was found for the slow/QK/IKVAV 3D scaffold than for the non-pro./QK/IKVAV 3D scaffold, the outer part of which appeared to show some initial signs of invasion. Finally, after 6 weeks, the pair of small longitudinal cylinders contained in both scaffolds showed almost complete invasion, thus leading to an anisotropic pattern. In addition, a delay in the invasion of the outer part of the non-pro./QK/IKVAV 3D scaffold was observed when compared to the slow/QK/IKVAV 3D scaffold, most likely due to its non-protease-sensitive nature (Figure 7a). In order to evaluate and quantify the cell-infiltration rate within the 3D scaffolds, DAPI counterstaining was performed. After 2 weeks, the stained slides revealed only limited cell infiltration for the outer part of the non-pro./QK/IKVAV 3D scaffold (Figure 7a). This contrasted with the outer part of the slow/QK/IKVAV 3D scaffold, which exhibited a higher cell colonization rate, in agreement with its protease-sensitive sequences. Furthermore, the two internal cylinders comprising the fast-QK and fast-IKVAV ELR hydrogels exhibited a significant increase in the number of cells, with no differences between them and the fabricated 3D scaffolds. This tendency continued at 4 and 6 weeks, with a higher density of blue stained cells for the outer part as well as for the inner pair of cylinders (Figure 7a). In addition, after 6 weeks, significant differences in cell density were found between the internal cylinders of the slow/QK/IKVAV 3D scaffold and the internal cylinders of the non-pro./QK/IKVAV 3D scaffold ($p < 0.001$), probably due to the faster cell colonization rate exhibited by the outer part of the slow/QK/IKVAV 3D scaffold. Thus, the specific preprogrammed configuration of the 3D scaffolds allowed a spatial and temporal control of cell infiltration, which resulted in an important contribution of an inside-to-outside pattern that contrast with the natural pattern observed for ordinary hydrogels.

The angiogenesis process within the 3D scaffolds was evaluated by anti-CD31 immunostaining, with the results showing no signs of CD31-positive cells until 4 weeks, when the outer parts of the non-pro./QK/IKVAV and slow/QK/IKVAV 3D scaffolds presented the same endothelial cell density as the internal cylinders bearing the fast-QK ELR hydrogels ($p > 0.05$) (Figure 7a,c). This endothelial invasion was restricted to the external areas in contact with the host tissue, with a lower endothelialization being found for the IKVAV-containing internal cylinders ($p < 0.001$). This trend continued after 6 weeks, with the lowest endothelial invasion being found for the outer part of the non-pro./QK/IKVAV 3D scaffold (Figure 7a,c). This was followed by the internal cylinders containing the fast-IKVAV hydrogel, with no significant differences ($p > 0.05$) between the two, and by the outer part of the slow/QK/IKVAV 3D scaffold, the higher vascularization of which is probably due to its more exposed configuration. In contrast, the internal cylinders bearing the fast-QK
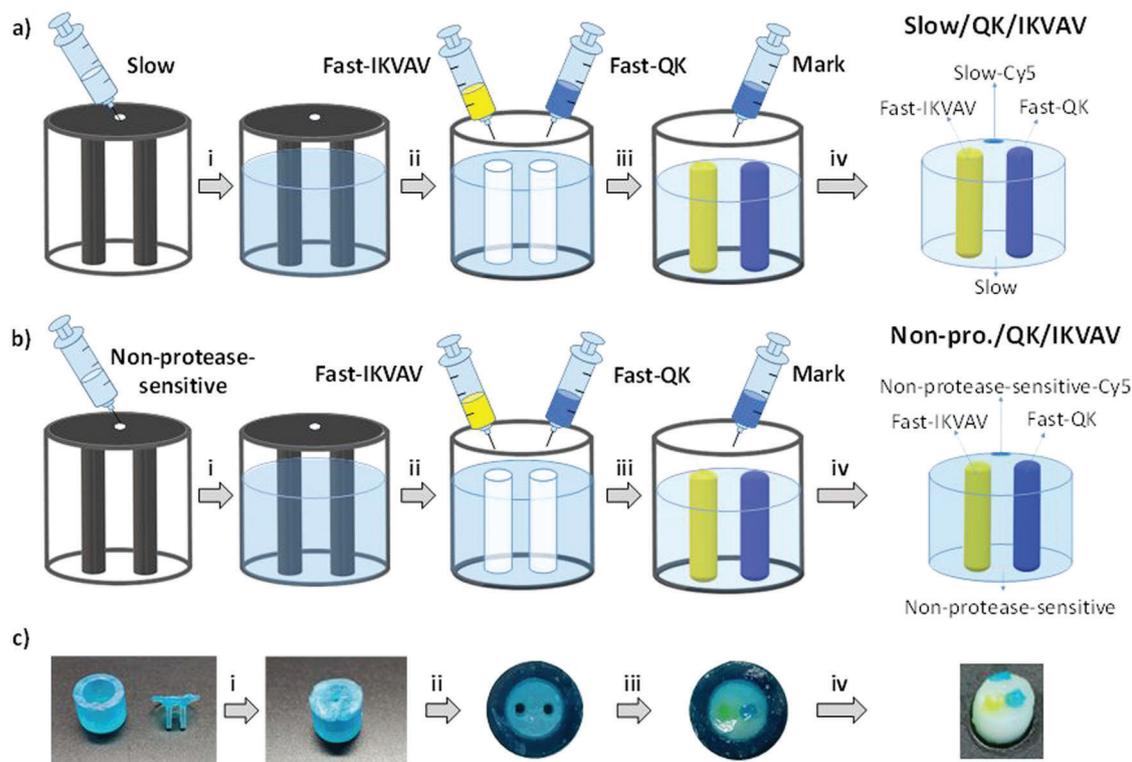
**ADVANCED
SCIENCE NEWS**

www.advancedsciencenews.com

**ADVANCED
HEALTHCARE
MATERIALS**

www.advhealthmat.de

Figure 6. Representative steps during formation of the a) slow/QK/IKVAV and b) Non-pro./QK/IKVAV 3D model ELR scaffolds. (i) Addition of slow or non-protease-sensitive ELR mixture (represented in light blue) and incubation for crosslinking at 4 °C during 10 min. (ii) Removal of the cap with the two coaxial mandrels. (iii) Deposition of fast-IKVAV (represented in yellow) and fast-QK hydrogel (represented in blue) on the left and right cylinders respectively, and incubation for crosslinking at 4 °C during 10 min. (iv) Addition of non-protease-sensitive-Cy5 or slow-Cy5 ELR mix on top of each respective construct to create a mark that differentiates the left and right cylinders, and incubation at 4 °C for 10 min. The construct is then detached from the mold to give the 3D scaffolds with the two internal cylinders left open to the surface, thus providing access to cells. c) Representative images during manufacture of the 3D model ELR scaffolds.

ELR hydrogels exhibited the highest vascularization, thus confirming the synergistic effect exerted by the QK peptide (covalently tethered) in combination with the uPA-protease-sensitive domains and leading to an anisotropic angiogenesis pattern (Figure 7a).

Anti-β-III tubulin immunofluorescence staining allowed the quantitative and qualitative evaluation of the innervation process within the 3D scaffolds. Herein, no presence of positive green staining for neuronal cells was observed until 6 weeks postimplantation (Figure 7a). Slides stained at this time point revealed a reduced neuronal infiltration for the outer parts of non-pro./QK/IKVAV and slow/QK/IKVAV 3D scaffolds, followed by the internal cylinders containing the fast-QK hydrogel. This contrasted with the marked invasion of neuronal cells observed for the internal cylinders bearing the fast-IKVAV ELR hydrogel in both 3D scaffolds, with a 4- to 5.7-fold increase when compared to the outer parts and QK-containing ELR hydrogels ($p < 0.001$) (Figure 7a,c). These results confirm that the combination of uPA-protease-sensitive domains and the IKVAV neuronal cell adhesion domain (covalently tethered) creates an anisotropic neuronal colonization pattern as a result of spatiotemporal control of the neurogenesis process. Figure 7b shows a close-up view of the capillaries and neuronal cells found in the inner QK- and IKVAV-containing ELR cylinders of the non-pro./QK/IKVAV and slow/QK/IKVAV 3D scaffolds.

As regards the development of strategies for the spatiotemporal control of angiogenesis, Yuen et al. described a three-layered cylindrical poly(lactic-*co*-glycolic) (PLG) scaffold embedding the VEGF factor in the central layer and anti-VEGF in the external layers.[28] Although this arrangement resulted in anisotropic vasculature formation in vivo, the significant variations in release rates observed may lead to malformations or tumor growths. In a subsequent study, our group created a coaxial binary ELR construct bearing the fast and slow uPA-protease-sensitive hydrogels on its inner and outer part, as well as the chemically tethered QK peptide.[14a] In this study, both factors showed a synergistic guidance of vascularization in the pre-programed arrangement, although the innervation process was overlooked.

In terms of the spatial and temporal direction of neurogenesis, Lampe et al. showed that lower crosslinking ratios and higher RGD densities in elastin-like protein (ELP) hydrogels resulted in a greater neurite extension in vitro.[29] Thus, upon careful selection of the material degradability and ligand cell-adhesive density, nerve fiber growth can be oriented in the three dimensions. In a different study, Farrukh et al. described the in situ light-based guidance of axonal growth on a IK(HANBP)VAV-modified Poly(acrylamide-*co*-acrylic acid)(PAAm-AA) hydrogel. Upon light exposure the photoremovable group 2-(4´-amino-4- nitro-[1,1´-biphenyl]-3-yl)propan-1-ol (HANBP) allowed the presentation of the IKVAV motif, thus directing the neurite outgrowth at
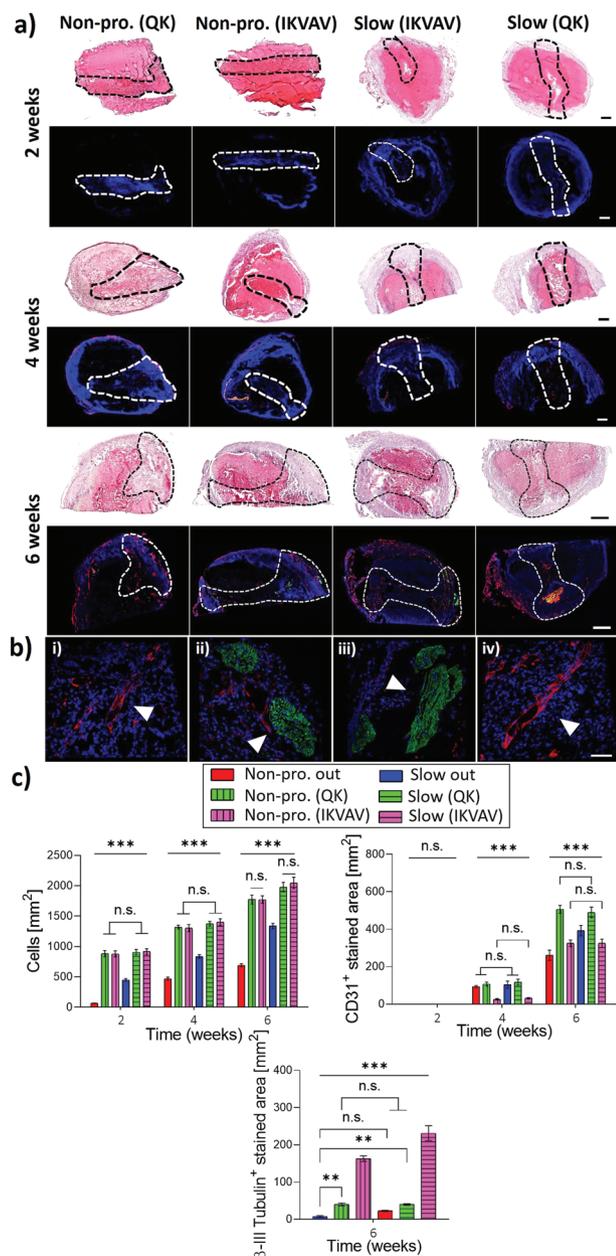
**ADVANCED
SCIENCE NEWS**

www.advancedsciencenews.com

**ADVANCED
HEALTHCARE
MATERIALS**

www.advhealthmat.de

Figure 7. Analysis of 3D model ELR scaffolds in vivo. a) Representative H&E stained ELR microsections with their corresponding CD31 and β-III tubulin immunofluorescence staining and DAPI counterstaining in black background. The nuclei appear in blue, endothelial cells in red and neuronal cells in green. The first two columns correspond to the non-pro./QK/IKVAV 3D model ELR scaffold, whereas the two last columns correspond to the slow/QK/IKVAV 3D model ELR scaffold. In addition, the first and fourth columns show the microsections containing the internal cylinder with the fast-QK hydrogel (surrounded by a black or white dotted line) and the second and third columns the microsections containing the internal cylinder with the fast-IKVAV hydrogel (surrounded by a black or white dotted line). Rows indicate time points. Scale bar = 500 μm. b) Representative magnified images of capillaries in red and neuronal cells in green found in the internal cylinders of non-pro./QK/IKVAV and slow/QK/IKVAV 3D scaffolds. (i) and (iv) correspond to the internal cylinders comprising fast-QK hydrogels, whereas (ii) and (iii) correspond to the internal cylinders comprising fast-IKVAV hydrogels. Structures are marked with white arrows. Scale bar = 50 μm. c) Quantification of number of cells,

the desired position.[11a] Although this study allowed a spatiotemporal control of axonal orientation, its applicability to 3D constructs in vivo has still to be confirmed. Similarly, Lopez-Silva et al. demonstrated that IKVAV-modified self-assembling multidomain peptide (MDP) hydrogels enhance neurite outgrowth in vitro and significantly accelerated remyelination and nerve regeneration in a rat sciatic nerve crush injury, thus supporting the IKVAV potential for 3D neurogenesis guidance in vivo.[30]

In contrast, herein we have developed 3D model ELR scaffolds bearing selected mechanobiological cues that provide an ECM-like environment, thus resulting in spatiotemporal guidance of angiogenesis and neurogenesis in vivo for use in advanced TERM applications.

3. Conclusion

The combination of protease-sensitive sequences with different degradation rates, the VEGF-mimetic peptide (QK) and the IK-VAV proneurogenesis peptide covalently tethered in a 3D model ELR scaffolds demonstrates, within the same scaffold, the preferential guidance of angiogenesis and neurogenesis in a spatiotemporal manner. The synergistic effect of protease-sensitive factors and biochemical signaling in cell infiltration, and subsequent preferential vascularization or innervation, was confirmed. Interestingly, the non-protease-sensitive or slow-protease-sensitive ELR hydrogel containing the pair of ELR cylinders allowed a highly defined one-directional pattern of vascularization and innervation in each cylinder, promoting a faster integration within the host tissue in the presence of the slow one. As such, we have shown that vascularization and innervation can be spatiotemporally controlled by selecting the bioactivities and degradation rates in a single ELR scaffold. The 3D model ELR scaffolds designed open up the possibility of novel strategies in tissue-engineering applications in which the spatiotemporal control of angiogenesis and neurogenesis, as well as the resorbable and nondegradable long-lasting nature of the bioinspired scaffold, play a paramount role.

4. Experimental Section

ELR Synthesis, Modification, and Characterization: ELR hydrogels and 3D model ELR scaffolds were manufactured from the previously described VKV-ELR, RGD-ELR, DRIR-ELR, and GTAR-ELR.[15a,20] VKV-ELR includes no bioactive domains, whereas RGD-ELR contains cell-adhesive RGD sequences, and DRIR-ELR and GTAR-ELR contain the slow (DRIR) and fast (GTAR) degrading sequences sensitive to the uPA enzyme (Table S3, Supporting Information), respectively. Recombinant techniques, along with the intrinsic thermoresponsiveness of ELRs in water, allow their bioproduction in *Escherichia coli* and purification by inverse transition cycling (ITC), respectively.[13b,31] Azide and cyclooctyne groups were selected as the crosslinking residues for formation of the ELR hydrogels. In this regard, azide groups were conjugated to the lysine amino acids interspersed

CD31$^+$-stained area and β-III tubulin$^+$-stained area per mm^2 found for the external part and internal cylinders of the 3D model ELR scaffolds at the different time points post-implantation. Some statistically significant comparisons are not shown for clarity. Data represented as ± SD. (***) $p < 0.001$, (**) $p < 0.01$, (*) $p < 0.05$ and (n.s.) no significant differences.

**ADVANCED
SCIENCE NEWS**

www.advancedsciencenews.com

**ADVANCED
HEALTHCARE
MATERIALS**

www.advhealthmat.de

within RGD-ELR and VKV-ELR to produce RGD-azide-ELR and VKV-azide-ELR. In the same vein, DRIR-cyclooctyne-ELR, GTAR-cyclooctyne-ELR, and VKV-cyclooctyne-ELR were prepared as the counterparts for the reaction via catalyst-free click chemistry.[15a,32] QK proangiogenic and IKVAV proneurogenesis peptides were attached to the RGD-azide-ELR via dibenzocyclooctyl (DBCO) group (Bachem, Switzerland), in a 0.5:1 and 1:1 proportion, respectively, to give RGD-azide-QK-ELR and RGD-azide-IKVAV-ELR, respectively. The 1:1 IKVAV:ELR ratio, or 60% w/w, was selected based on a previous study by Pavia dos Santos et al., which showed that a 20% w/w IKVAV ELR concentration (in reality 40%, as each ELR backbone contains two IKVAV domains) resulted in longer neurite formation than those containing 10% or 5% IKVAV-ELR.[33] An NHS-Cyanine 5 fluorescent probe (Jena Bioscience GmbH, Germany) was 1:1 conjugated to the RGD-azide-ELR and VKV-cyclooctyne-ELR to produce the RGD-azide-Cy5-ELR and VKV-cyclooctyne-Cy5-ELR. De novo produced ELRs, namely VKV-azide-ELR, VKV-azide-Cy5-ELR, RGD-azide-IKVAV-ELR, and RGD-azide-Cy5-ELR, were characterized by proton nuclear magnetic resonance (1H-NMR), matrix-assisted laser desorption/ionization time-of-flight mass spectrometry (MALDI-TOF), differential scanning calorimetry (DSC), and Fourier transform infrared spectroscopy (FTIR) (Figures S6–S21, Supporting Information).

Hydrogel Formation: Click-modified ELRs were dissolved in phosphate buffered saline (PBS) (pH 7.2, Gibco, USA) at 50 mg mL^{-1} 4 °C overnight (O/N), then mixed at a 1:1 volume ratio to produce the non-protease-sensitive (VKV-cyclooctyne-ELR + VKV-azide-ELR), slow (DRIR-cyclooctyne-ELR + VKV-azide-ELR), fast (GTAR-cyclooctyne-ELR + RGD-azide-ELR), fast-QK (GTAR-cyclooctyne-ELR + RGD-azide-QK-ELR), fast-IKVAV (GTAR-cyclooctyne-ELR + RGD-azide-IKVAV-ELR), slow-Cy5 (DRIR-cyclooctyne-ELR + RGD-azide-Cy5-ELR), and non-protease-sensitive-Cy5 (VKV-cyclooctyne-Cy5-ELR + VKV-azide-ELR) ELR hydrogels (Table S1, Supporting Information). Upon mixing, the temperature was maintained at 4 °C for 30 min to allow crosslinking of the polypeptide chains in their solvated state, thus obtaining homogeneous hydrogels.

Mechanical and Morphological Properties of the ELR Hydrogels: The elastic moduli of the ELR hydrogels were measured in triplicate by subjecting a sample, with a diameter of 12 mm and a volume of 260 µL, to a time-sweep experiment at 37 °C, 1% strain, 1 Hz frequency, 1000 µm gap, and soaked in PBS to avoid dehydration and shrinkage during the measurement (AR-2000ex rheometer, TA instruments, USA). The selected conditions correspond to the linear viscoelastic region of the hydrogel, as reported in Figures S1–S5 (Supporting Information). The porous microstructure of the cryo-fractured (liquid nitrogen), lyophilized, and gold sputter-coated hydrogels was examined by scanning electron microscopy (FEI Quanta 200FEG, Thermo Scientific, USA) and analyzed using the ImageJ software.[34]

Hydration Analysis of ELR Hydrogels: Hydration of ELR hydrogels was evaluated using the following equation (Equation (1))

$$\text{Gel hydration (\%)} = \left(\frac{W_1 - W_2}{\rho_{\text{water}}} \right) * \frac{100}{V_{\text{hydrogel}}} \tag{1}$$

where W_1 and V_{hydrogel} are the weight and volume of the hydrogel in the hydrated state, respectively; W_2 is the weight in the lyophilized state, and ρ_{water} is the density of water. Measurements were performed in triplicate.

Cell Culture: C6 glioma cells (ATCC CCL107, USA) were cultured in F12K Medium (ATCC 30-2004, USA) supplemented with 2.5% fetal bovine serum (FBS, Lonza, Switzerland) and 15% horse serum (Gibco, USA). Human umbilical vein endothelial cells (HUVECs; ATCC, PCS- 100-010) were cultured in EBM-2 basal medium (CC-3156, Lonza) supplemented with EGM-2 SingleQuots (CC-4176, Lonza), 100 µg mL^{-1} penicillin-streptomycin (Lonza) and 10% Fetal Bovine Serum (FBS, Lonza). Both types of cells were incubated at 37 °C in a 5% CO$_2$ humidified atmosphere. The medium was changed twice a week and cells were used at passages between 2 and 4 for subsequent experiments.

In Vitro C6 Glioma Cell Morphogenetic Analysis: A 2D in vitro system was used to analyze the morphogenic effect of ELR hydrogels on the C6 glial cells. Non-protease-sensitive, slow, fast, fast-QK, and fast-IKVAV hydrogels were prepared in a Millicell EZ slice 8-well (Thermo Scientific, USA) by depositing 20 µL of each hydrogel in different wells ($n = 3$). Subsequently, 10,000 C6 cells suspended in 200 µL of medium were seeded on top of the wells and incubated for 24, 48, and 72 h, at 37 °C and 5% CO$_2$. After each time point, hydrogels were fixed in 4% paraformaldehyde at room temperature (r.t.) for 2 h. Samples were then washed with PBS, permeabilized with 0.1% Triton X-100 (Sigma-Aldrich, USA) 30 min, blocked with BSA 1% (Sigma-Aldrich, USA) in PBS 1 h and stained with PBS solutions containing rhodamine-phalloidin (R415, Invitrogen, USA) and DAPI (1 µg mL^{-1}, Thermo Fisher, USA) for 30 min at r.t. DAPI-labeled nuclei appeared blue and phalloidin actin filaments appeared red. Subsequently, slides were sealed with a cover glass and fluorescence images obtained using an inverted Nikon Eclipse Ti-E epifluorescence microscope coupled to a DS-2MBWc camera using the NIS-Elements AR software (Nikon Corporation, Japan) and a Leica TCS SP8 LIGHTNING confocal microscope (Leica Microsystems, Germany). The length of the neurites was measured for a minimum of 12 random areas from different samples using the ImageJ software.

In Vitro Endothelial Cell Morphogenetic Analysis: In vitro vascularization analysis of the non-protease-sensitive, slow, fast, fast-QK, and fast-IKVAV hydrogels was performed in presence of HUVECs. In detail, 7000 HUVECs were suspended in 200 µL of medium, seeded on top of separately prepared 20 µL ELR hydrogels (Millicell EZ slice 8-well, Thermo Scientific, USA) and incubated for 2, 6, and 24 h, at 37 °C and 5% CO$_2$ ($n = 3$).[14a] After each time point, hydrogels were fixed in 4% paraformaldehyde at r.t. for 30 min. Samples were washed with PBS, permeabilized with 0.1% Triton X-100 (Sigma-Aldrich, USA) 30 min, blocked with BSA 1% (Sigma-Aldrich, USA) in PBS 1 h and stained with PBS solutions containing phalloidin-Alexa Fluor 488 (0.165 µm, Thermo Fisher, USA) and DAPI (1 µg mL^{-1}, Thermo Fisher, USA) for 30 min at r.t. DAPI-labeled nuclei appeared blue and phalloidin-labelled actin filaments appeared green. Subsequently, slides were sealed with a cover glass and fluorescence images acquired using an inverted Nikon Eclipse Ti-E epifluorescence microscope coupled to a DS-2MBWc camera using the NIS-Elements AR software (Nikon Corporation, Japan) and a Leica TCS SP8 LIGHTNING confocal microscope (Leica Microsystems, Germany). Cell spreading over time was evaluated by measuring the circularity ($4\pi*$area/perimeter^2) with the ImageJ software. Circularity values ranged from 0 (circle, nonelongated cell) to 1 (line, completely elongated cell),[14a] using a minimum of 12 random areas from different samples for quantification.

Preparation of 3D model ELR Scaffolds and ELR Hydrogels for the In Vivo Study: A description of the non-pro./QK/IKVAV and slow/QK/IKVAV 3D model ELR scaffolds with the ELR hydrogels forming their inner and outer parts can be found in Table S2 (Supporting Information). For preparation, a tubular mold (height = 0.6 cm, Ø = 0.5 cm) was used in combination with a cap displaying two coaxial mandrels (height = 0.6 cm, Ø = 0.1 cm) separated by 0.2 cm, designed to create the cavities necessary for manufacture of the inner pair of ELR hydrogels (Figure 6). First, 200 µL of non-protease-sensitive or slow ELR mixture was poured into the mold, the cap was attached and the ELR solution was crosslinked for 10 min at 4 °C. Subsequently, the cap was removed and 12 µL of fast-IKVAV or fast-QK ELR mix was poured into the left and right cavities, respectively, and incubated for 10 min at 4 °C. Finally, in order to differentiate the left and right ELR hydrogels, 2 µL of non-protease-sensitive-Cy5 or slow-Cy5 ELR mix was poured on top of each respective construct, and incubated for 10 min at 4 °C. Single non-protease-sensitive, slow, fast, fast-QK, and fast-IKVAV ELR hydrogels were manufactured by pouring 200 µL of each ELR mix into the cylindrical mold (height = 0.6 cm, Ø = 0.5 cm), and crosslinking for 10 min at 4 °C. All steps were conducted under sterile conditions.

Ethical Approval: Animal experiments were evaluated and approved by the Animal Care and Use Committee of the University of Valladolid in accordance with European Union Directive 2010/63/EU and Spanish Royal Decree RD 53/2013 (resolution number 7600394).

In Vivo Study: Female 3-month-old Swiss mice were selected and anesthetized with 3% isoflurane for the in vivo study. ELR hydrogels and 3D model ELR scaffolds were implanted subcutaneously in the lumbar region at both sides of the spinal cord, that is, two scaffolds per animal, and the wound was closed with absorbable sutures. Mice were provided with

water and food ad libitum, under 12:12 h light-dark cycles, and were euthanized with CO_2, collecting the scaffolds after 2, 4, and 6 weeks. Each condition was performed in triplicate using a total of 50 animals.

Sample Processing and Histology: ELR hydrogels and 3D model ELR scaffolds were extracted from the mice after 2, 4, and 6 weeks, introduced in optimum cutting temperature (OCT) mounting medium (VWR, USA) and frozen with liquid nitrogen-cooled 2-methylbutane (Sigma Aldrich, USA). 6 µm thick sections were cut at −20 °C in a cryostat (Shandon Cryotome E Cryostat, Thermo scientific, USA) and stained with H&E solutions (Sigma-Aldrich, USA) according to standard protocols.[35] Images were obtained using a bright-field optical microscope (Nikon Eclipse 80i, Japan) equipped with a color camera (Nikon Digital Sight DS-Fi1, Japan), using the NIS-Elements AR software (Nikon Corporation, Japan).

Immunohistochemistry: Frozen samples preserved in OCT were cut in a Shandon Cryotome E Cryostat (6 µm thick) and fixed in acetone (Sigma Aldrich, USA) for 2 min at −20 °C. Slices were thawed, rinsed three times in PBS and permeabilized with 0.1% Triton X-100 (Sigma-Aldrich, USA) at r.t. Subsequently, the cut sections were incubated in a humidified chamber with 10% normal goat serum (Life Technologies, USA) for 1 h at r.t., rinsed with PBS (3 times) and incubated O/N at 4 °C with anti-CD31 (endothelial cell labelling; ab28364, 1:50 dilution, Abcam, UK) and anti-β-III tubulin (neuronal marker; ab18207, 1:100, Abcam, UK) primary antibodies diluted in 1% normal goat serum (Dako, Denmark) in PBS. Secondary antibodies, namely goat anti-rabbit IgG H&L conjugated to Alexa Fluor 488 (ab150077, 1:500, Abcam, UK) and goat anti-rat IgG H&L conjugated to Alexa Fluor 546 diluted in 1% normal goat serum (in PBS), were added after three washing steps with PBS and incubated for 2 h at r.t. Sections were counterstained with Fluoroshield Mounting Medium containing DAPI (ab104139, Abcam, UK) and sealed with a cover glass. Negative controls, stained with secondary antibodies only, were also prepared. An inverted Nikon Eclipse Ti-E epifluorescence microscope coupled to a DS-2MBWc camera (Nikon Corporation, Japan) and a Leica TCS SP8 LIGHTNING confocal microscope (Leica Microsystems, Germany) were used to acquire the images. Pictures were converted to eight-bit images and thresholded using the ImageJ software. DAPI$^+$, CD31$^+$, and β-III tubulin$^+$ cells were manually quantified for a minimum of three randomly chosen areas of immunofluorescence stained images.

Statistical Analysis: One-way analysis of variance (ANOVA), with the Holm–Sidak method for post-hoc evaluation, was used to statistically analyze the gathered data (GraphPad Prism and Minitab v19.1, USA). Figures represent the mean and standard deviation for at least three different experiments whereas n.s. indicates no significant differences ($p \geq 0.05$), * indicates $p < 0.05$, ** $p < 0.01$, and *** $p < 0.001$.

Supporting Information

Supporting Information is available from the Wiley Online Library or from the author.

Conflict of Interest

The authors declare no conflict of interest.

Data Availability Statement

The data that support the findings of this study are available from the corresponding author upon reasonable request.

[1] a) C. Camaré, M. Pucelle, A. Nègre-Salvayre, R. Salvayre, *Redox Biol.* **2017**, *12*, 18; b) R. Roy, B. Zhang, M. A. Moses, *Exp. Cell Res.* **2006**, *312*, 608; c) S. S. Lakka, C. S. Gondi, J. S. Rao, *Brain Pathol.* **2005**, *15*, 327.

[2] a) J. Rouwkema, A. Khademhosseini, *Trends Biotechnol.* **2016**, *34*, 733; b) J. L. West, J. J. Moon, *Curr. Top. Med. Chem.* **2008**, *8*, 300; c) E. C. Novosel, C. Kleinhans, P. J. Kluger, *Adv. Drug Delivery Rev.* **2011**, *63*, 300.

[3] a) B. Z. Barkho, A. E. Munoz, X. Li, L. Li, L. A. Cunningham, X. Zhao, *Stem Cells* **2008**, *26*, 3139; b) L. Wojcik-Stanaszek, A. Gregor, T. Zalewska, *Acta Neurobiol. Exp.* **2011**, *71*, 103.

[4] a) J. R. Keast, *Organogenesis* **2013**, *9*, 168; b) H. Stoll, I. K. Kwon, J. Y. Lim, *Neural Regener. Res.* **2014**, *9*, 1810; c) X. Gu, F. Ding, D. F. Williams, *Biomaterials* **2014**, *35*, 6143.

[5] a) A. P. W. Johnston, S. A. Yuzwa, M. J. Carr, N. Mahmud, M. A. Storer, M. P. Krause, K. Jones, S. Paul, D. R. Kaplan, F. D. Miller, *Cell Stem Cell* **2016**, *19*, 433; b) A. Satoh, S. V. Bryant, D. M. Gardiner, *Dev. Biol.* **2012**, *366*, 374.

[6] V. Parfejevs, J. Debbache, O. Shakhova, S. M. Schaefer, M. Glausch, M. Wegner, U. Suter, U. Riekstina, S. Werner, L. Sommer, *Nat. Commun.* **2018**, *9*, 236.

[7] a) R. J. Kant, K. L. K. Coulombe, *Acta Biomater.* **2018**, *69*, 42; b) T. E. Brown, K. S. Anseth, *Chem. Soc. Rev.* **2017**, *46*, 6532; c) L. Havins, A. Capel, S. Christie, M. Lewis, P. Roach, *J. Neural Eng.* **2022**, *19*, 011001.

[8] a) S. Browne, A. Pandit, *Curr. Opin. Pharmacol.* **2017**, *36*, 34; b) V. Mastrullo, W. Cathery, E. Velliou, P. Madeddu, P. Campagnolo, *Front. Bioeng. Biotechnol.* **2020**, *8*, 188; c) K. F. Bruggeman, N. Moriarty, E. Dowd, D. R. Nisbet, C. L. Parish, *Br. J. Pharmacol.* **2019**, *176*, 355.

[9] a) K. Lee, E. A. Silva, D. J. Mooney, *J. R. Soc. Interface* **2011**, *8*, 153; b) M. M. Martino, S. Brkic, E. Bovo, M. Burger, D. J. Schaefer, T. Wolff, L. Gürke, P. S. Briquez, H. M. Larsson, R. Gianni-Barrera, R. Gianni-Barrera, J. A. Hubbell, A. Banfi, *Front. Bioeng. Biotechnol.* **2015**, *3*, 45; c) S. M. Eppler, D. L. Combs, T. D. Henry, J. J. Lopez, S. G. Ellis, J.-H. Yi, B. H. Annex, E. R. McCluskey, T. F. Zioncheck, *Clin. Pharmacol. Ther.* **2002**, *72*, 20; d) A. C. Lee, V. M. Yu, J. B. Lowe, M. J. Brenner, D. A. Hunter, S. E. Mackinnon, S. E. Sakiyama-Elbert, *Exp. Neurol.* **2003**, *184*, 295; e) R. Subbiah, R. E. Guldberg, *Adv. Healthcare Mater.* **2019**, *8*, 1801000.

[10] a) K. Tashiro, G. C. Sephel, B. Weeks, M. Sasaki, G. R. Martin, H. K. Kleinman, Y. Yamada, *J. Biol. Chem.* **1989**, *264*, 16174; b) A. Farrukh, F. Ortega, W. Fan, N. Marichal, J. I. Paez, B. Berninger, A. Del Campo, M. J. Salierno, *Stem Cell Rep.* **2017**, *9*, 1432.

[11] a) A. Farrukh, S. Zhao, J. I. Paez, A. Kavyanifar, M. Salierno, A. Cavalié, A. Del Campo, *ACS Appl. Mater. Interfaces* **2018**, *10*, 41129; b) B. Black, V. Vishwakarma, K. Dhakal, S. Bhattarai, P. Pradhan, A. Jain, Y. Kim, S. Mohanty, *Sci. Rep.* **2016**, *6*, 29876.

[12] a) A. Girotti, D. Orbanic, A. Ibáñez-Fonseca, C. Gonzalez-Obeso, J. C. Rodríguez-Cabello, *Adv. Healthcare Mater.* **2015**, *4*, 2423; b) D. W. Urry, T. M. Parker, M. C. Reid, D. C. Gowda, *J. Bioact. Compat. Polym.* **1991**, *6*, 263.

[13] a) D. W. Urry, C. H. Luan, T. M. Parker, D. C. Gowda, K. U. Prasad, M. C. Reid, A. Safavy, *J. Am. Chem. Soc.* **1991**, *113*, 4346; b) D. T. McPherson, J. Xu, D. W. Urry, *Protein Expr. Purif.* **1996**, *7*, 51.

**ADVANCED
SCIENCE NEWS**

www.advancedsciencenews.com

**ADVANCED
HEALTHCARE
MATERIALS**

www.advhealthmat.de

[14] a) F. González-Pérez, A. Ibáñez-Fonseca, M. Alonso, J. C. Rodríguez-Cabello, *Acta Biomater.* **2021**, *130*, 149; b) A. Ibáñez-Fonseca, S. Santiago Maniega, D. Gorbenko del Blanco, B. Catalán Bernardos, A. Vega Castrillo, Á. J. Á.l. Barcia, M. Alonso, H. J. Aguado, J. C. Rodríguez-Cabello, *Front. Bioeng. Biotechnol.* **2020**, *8*, 413; c) D.-M. Tian, H.-H. Wan, J.-R. Chen, Y.-B. Ye, Y. He, Y. Liu, L.-Y. Tang, Z.-Y. He, K.-Z. Liu, C.-J. Gao, S.-L. Li, Q. Xu, Z. Yang, C. Lai, X.-J. Xu, C.-S. Ruan, Y.-S. Xu, C. Zhang, L. Luo, L.-P. Yan, *Mater. Today Bio* **2022**, *15*, 100300.

[15] a) I. G. de Torre, M. Santos, L. Quintanilla, A. Testera, M. Alonso, J. C. R. Cabello, *Acta Biomater.* **2014**, *10*, 2495; b) H. C. Kolb, M. G. Finn, K. B. Sharpless, *Angew. Chem., Int. Ed.* **2001**, *40*, 2004.

[16] a) A. Ibáñez-Fonseca, T. Flora, S. Acosta, J. C. Rodríguez-Cabello, *Matrix Biol.* **2019**, *84*, 111; b) M. González-Pérez, D. B. Camasão, D. Mantovani, M. Alonso, J. C. Rodríguez-Cabello, *Biomater. Sci.* **2021**, *9*, 3860; c) P. Contessotto, D. Orbanić, M. Da Costa, C. Jin, P. Owens, S. Chantepie, C. Chinello, J. Newell, F. Magni, D. Papy-Garcia, *Sci. Transl. Med.* **2021**, *13*, eaaz5380; d) A. Fernández-Colino, F. Wolf, R. Moreira, S. Rütten, T. Schmitz-Rode, J. C. Rodríguez-Cabello, S. Jockenhoevel, P. Mela, *Eur. Polym. J.* **2019**, *121*, 109334; e) F. Chen, P. Le, G. M. Fernandes-Cunha, S. C. Heilshorn, D. Myung, *Biomaterials* **2020**, *255*, 120176; f) A. Ibáñez-Fonseca, T. L. Ramos, I. Gonzalez de Torre, L. I. Sánchez-Abarca, S. Muntión, F. J. Arias, M. C. Del Cañizo, M. Alonso, F. Sánchez-Guijo, J. C. Rodríguez-Cabello, *J. Tissue Eng. Regener. Med.* **2018**, *12*, e1450; g) A. Fernández-Colino, F. Wolf, S. Rütten, T. Schmitz-Rode, J. C. Rodríguez-Cabello, S. Jockenhoevel, P. Mela, *Front. Bioeng. Biotechnol.* **2019**, *7*, 340.

[17] a) T. Flora, I. G. de Torre, M. Alonso, J. C. Rodríguez-Cabello, *J. Mater. Sci. Mater. Med.* **2019**, *30*, 30; b) L. D. D'Andrea, G. Iaccarino, R. Fattorusso, D. Sorriento, C. Carannante, D. Capasso, B. Trimarco, C. Pedone, *Proc. Natl. Acad. Sci. USA* **2005**, *102*, 14215; c) S. E. D'Souza, M. H. Ginsberg, E. F. Plow, *Trends Biochem. Sci.* **1991**, *16*, 246; d) S. M. Staubli, G. Cerino, I. G. De Torre, M. Alonso, D. Oertli, F. Eckstein, K. Glatz, J. C. R. Cabello, A. Marsano, *Biomaterials* **2017**, *135*, 30.

[18] a) L. L. Y. Chiu, M. Radisic, *Biomaterials* **2010**, *31*, 226; b) P. R. Kuhl, L. G. Griffith-Cima, *Nat. Med.* **1996**, *2*, 1022; c) L. L. Y. Chiu, R. D. Weisel, R. Li, M. Radisic, *J. Tissue Eng. Regener. Med.* **2011**, *5*, 69; d) L. Cai, C. B. Dinh, S. C. Heilshorn, *Biomater. Sci.* **2014**, *2*, 757.

[19] a) B. P. Dos Santos, B. Garbay, M. Fenelon, M. Rosselin, E. Garanger, S. Lecommandoux, H. Oliveira, J. Amédée, *Acta Biomater.* **2019**, *99*, 154; b) K. S. Straley, S. C. Heilshorn, *Soft Matter* **2009**, *5*, 114.

[20] T. Flora, I. G. De Torre, M. Alonso, J. C. Rodríguez-Cabello, *Biofabrication* **2019**, *11*, 035008.

[21] a) R. Pittier, F. Sauthier, J. A. Hubbell, H. Hall, *J. Neurobiol.* **2005**, *63*, 1; b) M. A. R. Dent, Y. Sumi, R. J. Morris, P. J. Seeley, *Eur. J. Neurosci.* **1993**, *5*, 633.

[22] a) S. J. Hollister, *Nat. Mater.* **2005**, *4*, 518; b) A. J. Engler, S. Sen, H. L. Sweeney, D. E. Discher, *Cell* **2006**, *126*, 677.

[23] L. Mbundi, M. González-Pérez, F. González-Pérez, D. Juanes-Gusano, J. C. Rodríguez-Cabello, *Front. Mater.* **2021**, *7*, 601795.

[24] E. Ruoslahti, M. D. Pierschbacher, *Science* **1987**, *238*, 491LP.

[25] a) X. Lin, K. Takahashi, Y. Liu, P. O. Zamora, *Biochim. Biophys. Acta, Gen. Subj.* **2006**, *1760*, 1403; b) J. P. Jung, A. K. Nagaraj, E. K. Fox, J. S. Rudra, J. M. Devgun, J. H. Collier, *Biomaterials* **2009**, *30*, 2400.

[26] Y. Li, M. D. Hoffman, D. S. W. Benoit, *Biomaterials* **2021**, *268*, 120535.

[27] J. E. Leslie-Barbick, J. E. Saik, D. J. Gould, M. E. Dickinson, J. L. West, *Biomaterials* **2011**, *32*, 5782.

[28] W. W. Yuen, N. R. Du, C. H. Chan, E. A. Silva, D. J. Mooney, *Proc. Natl. Acad. Sci. USA* **2010**, *107*, 17933.

[29] K. J. Lampe, A. L. Antaris, S. C. Heilshorn, *Acta Biomater.* **2013**, *9*, 5590.

[30] T. L. Lopez-Silva, C. D. Cristobal, C. S. E. Lai, V. Leyva-Aranda, H. K. Lee, J. D. Hartgerink, *Biomaterials* **2021**, *265*, 120401.

[31] A. Girotti, J. Reguera, J. C. Rodríguez-Cabello, F. J. Arias, M. Alonso, A. M. Testera, *J. Mater. Sci. Mater. Med.* **2004**, *15*, 479.

[32] N. J. Agard, J. A. Prescher, C. R. Bertozzi, *J. Am. Chem. Soc.* **2004**, *126*, 15046.

[33] B. P. dos Santos, B. Garbay, M. Pasqua, E. Chevron, Z. S. Chinoy, C. Cullin, K. Bathany, S. Lecommandoux, J. Amédée, H. Oliveira, *J. Biotechnol.* **2019**, *298*, 35.

[34] C. T. Rueden, J. Schindelin, M. C. Hiner, B. E. DeZonia, A. E. Walter, E. T. Arena, K. W. Eliceiri, *BMC Bioinformatics* **2017**, *18*, 529.

[35] A. H. Fischer, K. A. Jacobson, J. Rose, R. Zeller, *Cold Spring Harb. Protoc.* **2008**, *2008*, pdb.prot4986.

2201646 (11 of 11)